Conference on Modelling Fluid Flow (CMFF'18)
The 17th International Conference on Fluid Flow Technologies
Budapest, Hungary, September 4-7, 2018

Multiphase Model to Predict Many Gravel Particles Transported by Free-Surface Flows

Satoru USHIJIMA[1], Daisuke TORIU[2], Hirofumi YANAGI[3]

[1] Corresponding Author. Academic Center for Computing and Media Studies (ACCMS), Kyoto University. Yoshida-Honmachi, Sakyo-ku, Kyoto-shi, 606-8501, Japan. E-mail: ushijima.satoru.3c@kyoto-u.ac.jp
[2] Academic Center for Computing and Media Studies (ACCMS), Kyoto University. Yoshida-Honmachi, Sakyo-ku, Kyoto-shi, 606-8501, Japan. E-mail: toriu.daisuke.8v@kyoto-u.ac.jp
[3] CERE, Graduate School of Engineering, Kyoto University. 615-8540, Japan.

ABSTRACT

A parallel computation method with a multiphase model was applied to the local scour and deposition of a gravel bed, consisting of about 17,000 non-spherical gravel particles with a diameter of around 7 mm, caused by falling overflows over a rectangular-notch weir. In the computations, representative 26 shapes of gravel particles were determined from actual particles, each of which was represented with tetrahedron elements. The fluid forces acting on a non-spherical gravel particle were estimated with the volume integral of the pressure and viscosity terms included in phase-averaged momentum equations for the gas and liquid flows. In addition, the particle-particle interactions were taken into account with multiple contact-detection spheres placed inside of a particle model used in computations. In comparison with the experimental results, it was shown that the dynamic behaviors and the deformation of the gravel bed, including the horizontal distribution not indicated in our previous study [1], are reasonably predicted with the present computation method.

Keywords: fluid-solid interaction, free-surface flow, non-spherical gravel particle transportation, multiphase model, parallel computation

NOMENCLATURE

$\boldsymbol{F}_F$	$[N]$	fluid force acting on solid model
$\boldsymbol{F}_C$	$[N]$	contact force acting on solid model
g	$[m/s^2]$	gravity acceleration
g_i	$[m/s^2]$	external acceleration in x_i
$\boldsymbol{I}$	$[kg/m^2]$	inertia tensor
M_b	$[kg]$	mass of solid model
$\boldsymbol{N}$	$[N \cdot m]$	external torque
p	$[Pa]$	volume-average pressure
R	$[-]$	rotation matrix
t	$[s]$	time
$u_{b,i}$	$[m/s]$	u_i interpolated on cell boundary
u_i	$[m/s]$	mass-average velocity in x_i
u_i^*	$[m/s]$	tentative u_i
$\tilde{u}_i$	$[m/s]$	velocity defined in Eq.(6)
$u_{i,k}$	$[m/s]$	u_i in phase$-k$
$\boldsymbol{v}$	$[m/s]$	velocity vector of solid model
x_i	$[m]$	orthogonal coordinates
γ_1, γ_2	$[-]$	parameters in Eq.(5)
Δm	$[kg]$	mass of solid model in cell
Δt	$[s]$	time increment
μ	$[kg/(m \cdot s)]$	viscous coefficient for fluid
ρ	$[kg/m^3]$	density averaged for fluid
ρ_b	$[kg/m^3]$	density for fluid and solid
ρ_k	$[kg/m^3]$	ρ in phase$-k$
ϕ	$[Pa]$	$p^{n+1} - p^n$
Ω	$[-]$	cell volume
Ω_k	$[-]$	volume fraction of phase$-k$
$\boldsymbol{\omega}$	$[1/s]$	angular velocity vector

1. INTRODUCTION

Fluid-solid and solid-solid interactions are of great importance to numerically predict the movements of solid particles transported by the flows having largely deformed free-surfaces, such as the gravel particles moved by falling overflows and so-called dam-break flows. The present computation method is based on a phase-averaged model, in which governing equations of incompressible and immiscible gas and liquid phases are transformed into the phase-averaged equations [2].

Regarding the numerical simulation for gravel particle transportations, there have been several studies so far; for example, the movements of many sphere particles have been calculated with an immersed boundary method [3] and the particles represented by "connected spheres" have been calculated [4] with the computation method similar to our method originally proposed by us in 2008 [5].

In this study, the governing equations for flu-

ids (gas and liquid phases) are solved with a finite volume method in the Eulerian grid, which is decomposed into multiple subdomains for parallel computations. To solve the governing equations for fluids, an effective implicit method (C-ISMAC method) [6] is employed. The C-ISMAC method allows us to use arbitrary higher-order schemes for convection and diffusion terms as well as to decrease the elapsed time due to the effect of implicit discretization. In addition, in order to satisfy the incompressible condition accurately, pressure-Poisson equations are solved with the C-HSMAC method [7], which is much useful compared with usual SOLA and HSMAC methods [8] in terms of computational efficiency.

A solid model used in the computations consists of multiple tetrahedron elements to represent its shape as correctly as possible, so that the inertial tensor and other physical properties can be treated accurately. The translational and rotational motions of the solid models are calculated in a Lagrangian way. The fluid forces acting on a solid model are estimated from the volume integral of the pressure and viscous terms in the phase-averaged momentum equations of the fluids. The above treatment for solid model is largely effective compared with the other methods, in which gravel particles are represented by spheres or "connected sphere" models.

The present method was applied to the transportation of about 17,000 gravel particles caused by the falling water through a weir. The plan views of deformed gravel beds were measured and compared with calculations, which were not included in our previous study [1]. The validity of the present computation method will be discussed in comparison with the experimental results.

2. NUMERICAL PROCEDURES

2.1. Multiphase Model

As schematically shown in Fig. 1, the present method deals with the multiphase field consisting of gas, liquid and solid phases, where each phase is assumed to be incompressible and immiscible. In Fig. 1, Ω and Ω_k stand for the volumes of a computational cell and that of the phase-k respectively, where $\Omega = \sum_k \Omega_k$.

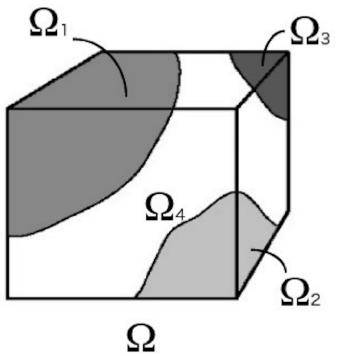

Figure 1. Multiphase field in a fluid cell

Taking account of the incompressibility, a set of phase-averaged governing equations can be obtained for gas and liquid phases [2]. As shown below, they consist of incompressible condition, conservation equations of mass and momentum :

$$\frac{\partial u_i}{\partial x_i} = 0 \tag{1}$$

$$\frac{\partial \rho}{\partial t} + \frac{\partial (\rho u_i)}{\partial x_i} = 0 \tag{2}$$

$$\frac{\partial u_i}{\partial t} + \frac{\partial (u_i u_j)}{\partial x_j} = -\frac{1}{\rho}\frac{\partial p}{\partial x_i} + g_i + \frac{1}{\rho}\frac{\partial}{\partial x_j}\left[\mu\left(\frac{\partial u_i}{\partial x_j} + \frac{\partial u_j}{\partial x_i}\right)\right] \tag{3}$$

where t is time, x_i is the i-th component of three-dimensional orthogonal coordinates and g_i is the acceleration of external force in x_i direction. While the velocity component u_i is the mass-averaged value in the mixture of fluids, volume-averaged variables are used for the other variables and a physical property, density ρ, pressure p and viscous coefficient μ. For example, a mass-averaged velocity component u_i is defined with the densities ρ_k as

$$u_i = \frac{\sum_k \rho_k \Omega_k u_{i,k}}{\sum_k \rho_k \Omega_k} \tag{4}$$

In the present computations, Ω_k is estimated with the sub-cell method [9].

2.2. Computations of Gas and Liquid Phases

The governing equations are discretized with a finite volume method on collocated-grid system. In the fluid computations, a tentative velocity component u_i^* is calculated with p^n at the collocated grid point located at the center in a fluid cell, where all velocity components and scalar variables are defined. In this procedure, Eq.(3) is discretized with an implicit method, proposed as a C-ISMAC method [6]. First, the discretized momentum equation is given by

$$\begin{aligned}\frac{u_i^* - u_i^n}{\Delta t} &= g_i - \frac{1}{\rho}\frac{\partial p^n}{\partial x_i} \\ &- \gamma_1 \frac{\partial}{\partial x_j}(u_i^* u_j^n) - (1-\gamma_1)\frac{\partial}{\partial x_j}(u_i^n u_j^n) \\ &+ \frac{\gamma_2}{\rho}\frac{\partial}{\partial x_j}\left[\mu\left(\frac{\partial u_i^*}{\partial x_j} + \frac{\partial u_j^*}{\partial x_i}\right)\right] \\ &+ \frac{1-\gamma_2}{\rho}\frac{\partial}{\partial x_j}\left[\mu\left(\frac{\partial u_i^n}{\partial x_j} + \frac{\partial u_j^n}{\partial x_i}\right)\right]\end{aligned} \tag{5}$$

where γ_1 and γ_2 are parameters within $0 \le \gamma_1, \gamma_2 \le 1$. Second, the tentative velocity component u_i^* is assumed to be given by the following relationship :

$$u_i^* = u_i^n + \tilde{u}_i \tag{6}$$

Finally, substituting Eq.(6) into Eq.(5), the following equation is derived :

$$\frac{\tilde{u}_i}{\Delta t} + \gamma_1 \frac{\partial}{\partial x_j}(\tilde{u}_i u_j^n) - \frac{\gamma_2}{\rho}\frac{\partial}{\partial x_j}\left[\mu\left(\frac{\partial \tilde{u}_i}{\partial x_j} + \frac{\partial \tilde{u}_j}{\partial x_i}\right)\right] = g_i - \frac{1}{\rho}\frac{\partial p^n}{\partial x_i} - \frac{\partial}{\partial x_j}(u_i^n u_j^n) + \frac{1}{\rho}\frac{\partial}{\partial x_j}\left[\mu\left(\frac{\partial u_i^n}{\partial x_j} + \frac{\partial u_j^n}{\partial x_i}\right)\right] \tag{7}$$

where the unknown component $\tilde{u}_i$ should be smaller than u_i^n in case that the time-scale of the flow field is sufficiently larger than the time increment Δt used in calculations. Thus, we can apply a simple first-order spatial discretization method to the left-hand side of Eq.(7), while a higher-order scheme to the dominant right-hand side. In this study, the latter convection terms are calculated with a fifth-order TVD scheme [10].

The above C-ISMAC method allows us to use relatively large Courant number due to the implicit characteristics as shown on the left-hand side of Eq.(7) as well as to preserve high numerical accuracy by applying a higher-order scheme to the dominant convection terms on the right-hand side of Eq.(7). The mass conservation equation given by Eq.(2) is also solved with the C-ISMAC method in the same way as shown above.

After solving the linear equation system of $\tilde{u}_i$ obtained from the spatial discretization of Eq.(7), u_i^* is determined with Eq.(6). In the pressure computation stage, u_i^* located at the center in fluid cells are spatially interpolated on the cell boundaries to $u_{b,i}$. Using $u_{b,i}$, the following equation, corresponding to a pressure Poisson equation in an incompressible fluid, is derived with Eq.(1) :

$$\frac{\partial}{\partial x_i}\left(\frac{1}{\rho}\frac{\partial \phi^k}{\partial x_i}\right) = \frac{1}{\Delta t}\frac{\partial u_{b,i}}{\partial x_i} \equiv \frac{D}{\Delta t} \tag{8}$$

where $\phi = p^{n+1} - p^n$.

In the pressure computation stage, Eq.(8) is solved with the C-HSMAC method [11]. The iterative procedure in the C-HSMAC method is shown as follows :

do $k = 1, 2, \cdots, k_m$ until all $|D^k| < \epsilon_D$

$$\frac{\partial}{\partial x_i}\left(\frac{1}{\rho}\frac{\partial \phi}{\partial x_i}\right) = \frac{D^k}{\Delta t} \tag{9}$$

$$p^{k+1} = p^k + \phi \tag{10}$$

$$u_{b,i}^{k+1} = u_{b,i}^k - \frac{\Delta t}{\rho}\frac{\partial \phi}{\partial x_i} \tag{11}$$

enddo

The above C-HSMAC method enables us to obtain u_i^* that satisfies the incompressible condition, $|D^k| < \epsilon_D$, in all computational cells, where ϵ_D is an appointed threshold. While the pressure p^{k+1} is not directly used in the above iterative calculations, it becomes the new time-step pressure, p^{n+1}, after the iterative procedures in the C-HSMAC method. As a similar method to the C-HSMAC method, the SOLA or HSMAC method has been proposed [12]. However, it was confirmed that the computational efficiency of the C-HSMAC method is largely improved compared with SOLA [13].

2.3. Computations of Solid Model

The solid objects transported by gas and liquid flows are assumed to be rigid bodies which have no deformation due to the collision with the other solid objects. In the present computation method, the actual solid object is represented by multiple tetrahedron elements as shown in Fig. 2. The contact forces between solid objects are estimated using multiple contact-detection spheres set up inside of the solid model as shown in Fig. 3. The normal and tangential forces arising in the contact spheres are calculated on the basis of a distinct element method (DEM) [14].

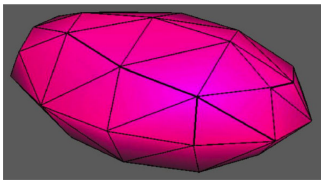

Figure 2. Solid model represented by multiple tetrahedron elements

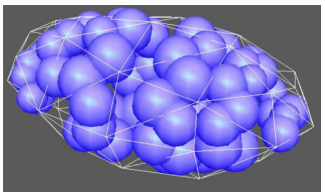

Figure 3. Contact-detection spheres

The movements of the solid models are calculated with the governing equations for translational and rotational motions. The momentum equation of the translational motion is given by

$$M_b \dot{\boldsymbol{v}} = \boldsymbol{F}_F + \boldsymbol{F}_C \tag{12}$$

where M_b is the mass of the solid model, $\boldsymbol{v}$ is the velocity vector of its center and dot means time differentiation. On the right hand side of Eq.(12), fluid force $\boldsymbol{F}_F$ and contact force $\boldsymbol{F}_C$ are taken into account. The governing equation of the rotational motion, which is called Euler equation, is given by

$$\dot{\boldsymbol{\omega}} = \boldsymbol{I}^{-1}\left[R^{-1}\boldsymbol{N} - \boldsymbol{\omega} \times \boldsymbol{I}\boldsymbol{\omega}\right] \tag{13}$$

where $\boldsymbol{\omega}$ is the angular velocity vector, $\boldsymbol{I}$ is the inertia tensor calculated with the tetrahedron elements of the object, R is a rotation matrix and $\boldsymbol{N}$ is the external torque resulting from $\boldsymbol{F}_F$ and $\boldsymbol{F}_C$. The calculation related to the rotation is actually performed with quaternion instead of the multiplication of the rotation matrix R. The location and posture of the solid model are determined form Eqs.(12) and (13). The

x_i component of the fluid force f_{Fi}, which acts on a part of an object included in a fluid cell in the finite volume method, is calculated with the pressure and viscous terms of Eq. (3) :

$$f_{Fi} = \Delta m \left[-\frac{\rho_b - \rho_f}{\rho_b} g \delta_{3i} - \frac{1}{\rho_b} \frac{\partial p}{\partial x_i} + \frac{1}{\rho_b} \frac{\partial}{\partial x_j} \left\{ \mu \left(\frac{\partial u_i}{\partial x_j} + \frac{\partial u_j}{\partial x_i} \right) \right\} \right] \quad (14)$$

where Δm is the mass of the object included in a fluid cell and ρ_b is the volume-average density of fluids and solid model partially included in a fluid cell. With x_3 axis vertically upward, g is the acceleration of gravity and δ_{3i} is a Kronecker delta. The summation of f_{Fi} over all fluid cells including the same solid model corresponds to the component of the fluid force $\boldsymbol{F}_F$ on the right hand side of Eq. (12). The volume fraction of solid models included in a computational cell is estimated with a sub-cell method [9].

2.4. Parallel Computations

The present computation method is based on an Eulerian-Lagrangian method for the computations of fluids and solid models. The computation method is completely parallelized with flat MPI (Message-Passing Interface) [15] on the basis of a three-dimensional domain decomposition method.

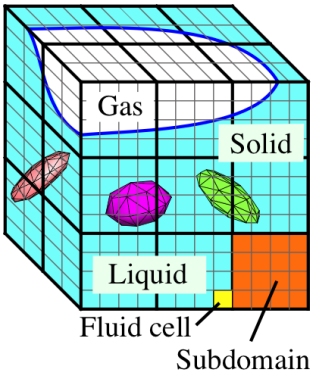

Figure 4. Schematic view of computational region

Figure 4 shows the schematic view of the computational region in this method. The governing equations for gas and liquid phases are discretized in the Eulerian fluid cells with a finite volume method, while the movements of the solid models are treated in a Lagrangian way on the Eulerian fluid cells. As shown in Fig. 4, the Eulerian cells are decomposed into multiple subdomains for parallel computations. In the fluid computations, the overlapping regions are set up around the subdomain as illustrated in 5, in order to store the necessary variables which are exchanged between subdomains with MPI. In the similar way, the necessary data on the solid models are exchanged with the different overlapping areas which are able to include the maximum solid models.

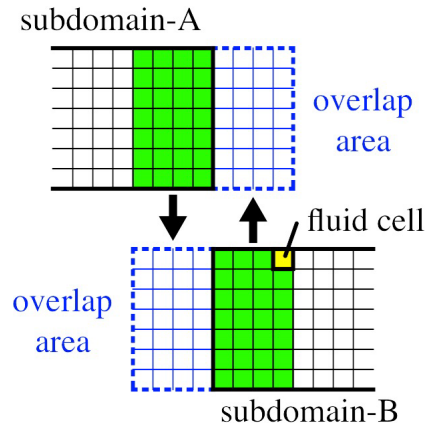

Figure 5. Message passing in fluid computations

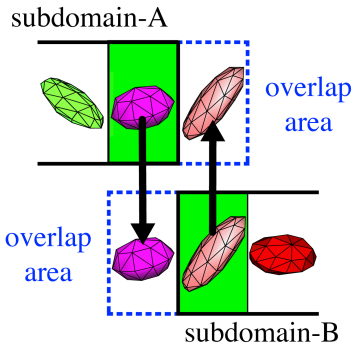

Figure 6. Message passing on solid model

The computations in the following part of this paper were conducted with supercomputer systems in Kyoto University (Xeon Broadwell 2.1GHz 18 cores×2, 128 GB memory [per node] × 850 [nodes] and other systems).

2.5. Grid Resolution and Drag Force

In our preceding studies [5], the drag coefficient and wake flows behind a cylindrical structure were calculated in order to confirm the validity of the present method. In the computations, the lengths of the three-dimensional rectangular computational domain were 1.2 $[m] \times 0.8$ $[m] \times 0.5$ $[m]$ in $x_1 \times x_2 \times x_3$ directions, where x_1, x_2 and x_3 are streamwise, transverse and vertical directions respectively. The vertical cylinder 0.1 $[m]$ in diameter D was represented with 898 tetrahedron elements and placed in the domain where the uniform inlet velocity U was set on the upstream surface at $x_1 = 0$. Since the number of the fluid cells was $120 \times 80 \times 50$ in $x_1 \times x_2 \times x_3$ directions respectively, the volume of the cylinder with the unit axial length ($= 100\pi/4$ $[cm^3]$) includes about 78.5 fluid cells ($= 1$ $[cm^3]$) in terms of the volumetric grid resolution.

Figure 7 shows the wake flows behind the cylinder with different Reynolds number Re_d, which is defined by $Re_d = UD/\nu$. In the experiments as shown by Chen [16] and others, it is known that the 2D steady wake flows change to 2D unsteady ones when Re_d is greater than around 40 and that the un-

steady 2D wake flows become 3D ones when Re_d is greater than around 150. The similar tendencies can be confirmed in the calculated results with the present method as shown in Fig. 7.

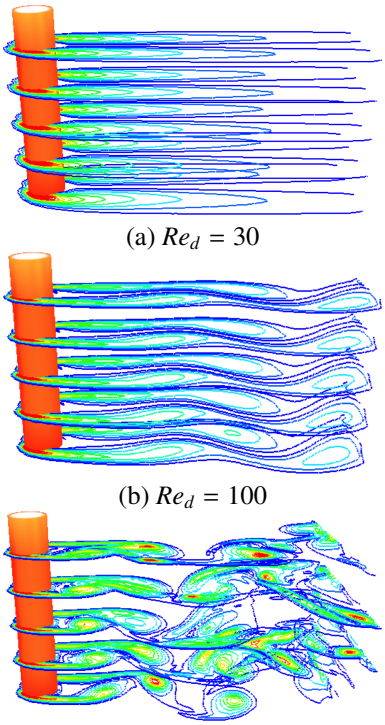

(a) Re_d = 30

(b) Re_d = 100

(c) Re_d = 300

Figure 7. Calculated vorticities in wake flows

Figure 8 shows the relationship between Re_d and drag coefficient Cd obtained from the calculated fluid forces acting on the cylinder. As far as the range of Re_d shown in Fig. 8 is concerned, the present grid resolution is sufficient to obtain the reasonable computational results which agree well with the experimental values. In addition, the applicability of the present method to more complicated-shaped structures were shown in our preceding studies [17].

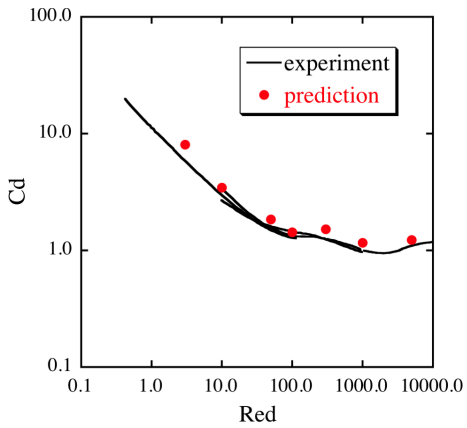

Figure 8. Relationship between Re_d and Cd

3. APPLICATION OF COMPUTATION METHOD

3.1. Gravel Particle Model

In an attempt to determine the shapes of the solid models used in computations, 500 actual gravel particles with a mean diameter of about 7 mm were randomly selected and their diameters a, b and c illustrated in Fig. 9 were measured. On the basis of the measured diameters, different 26 shapes of the solid models and their distribution were determined. Each solid model is represented with multiple tetrahedron elements and includes contact-detection spheres as shown in Figs. 2 and 3. The solid models with different shapes will be shown in different colors in the following results.

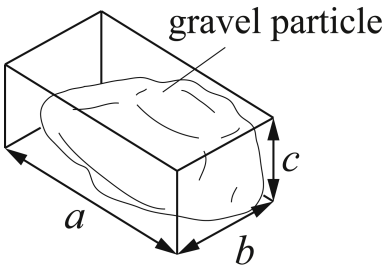

Figure 9. Diameters (a, b and c) of actual gravel particle

3.2. Angle of Repose

In order to confirm the effects of the present solid models, the angle of repose of the gravel particles in water were calculated and the results were compared with the experimental results.

The experimental equipment is shown in Fig. 10. The actual gravel particles were initially placed in the regions indicated in Fig. 10. When the partition plate is removed, gravel particles supported by the plate slide into the other side. The angle of repose can be found in the stationary results.

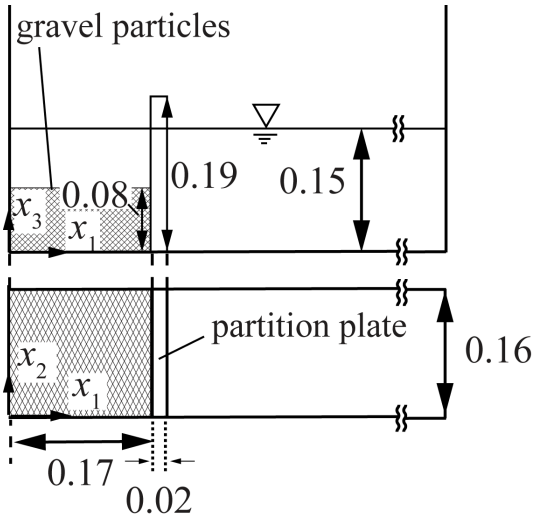

Figure 10. Experimental equipment to observe angle of repose (unit [m])

Meanwhile in the computations, initially about 6,700 solid models were randomly placed in the rectangular region, whose geometry is almost same as the experiments shown in Fig. 10. Similarly to the experiments, one side of the walls surrounding the solid models was released and their movements were calculated until the steady state was obtained with 180 parallel computations. Since the solid models are in the water with a free surface, the fluid behaviors were also calculated in addition to the computations of solid models.

In the computations, on the wall boundaries, non-slip conditions were set for the velocity components parallel to the walls, while pressure boundary conditions were given by $\partial p/\partial n = 0$ on all wall boundaries. Regarding the boundary conditions for solid models, normal and tangential forces act on them through the contact-detection spheres shown in Fig. 3 on all wall boundaries.

Figure 11 shows the stationary distributions of the solid models in calculations and actual gravel particles in experiments. In Fig. 11, the top figure shows the results obtained with "sphere solid models", while the middle figure shows the results with the present solid models having 26 different non-spherical shapes. Compared with the experimental results shown in the bottom of Fig. 11, it is clear that the distributions of the present solid models agree well with the experimental ones.

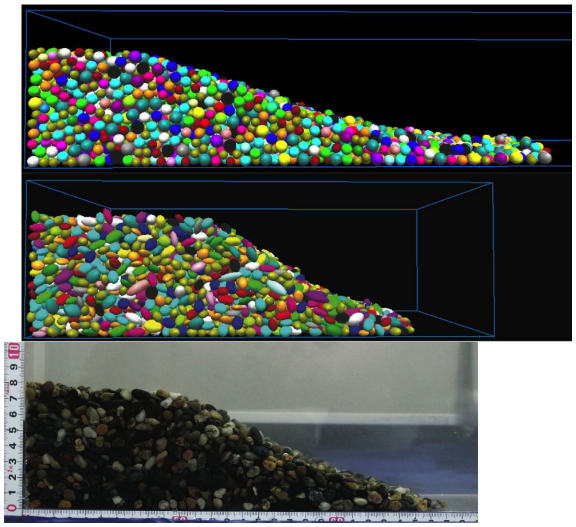

Figure 11. Distribution of particles (top: sphere solid model, middle: present solid model, bottom: experimental result)

In addition, Fig. 12 shows the quantitative comparisons of the particle bed heights. The experimental results in Fig. 12 are shown with error bars, which mean the variation of five times measurements, as well as shown with their averaged values. From the results shown in Fig. 12, it is obvious that the present solid models which have 26 different shapes determined from the actual gravel particles are in good agreement with the experiments compared with the calculated results with sphere models. Thus, it can be concluded that the modelling of the gravel particle shapes is important to predict their transportations especially on the largely undulating bed profiles.

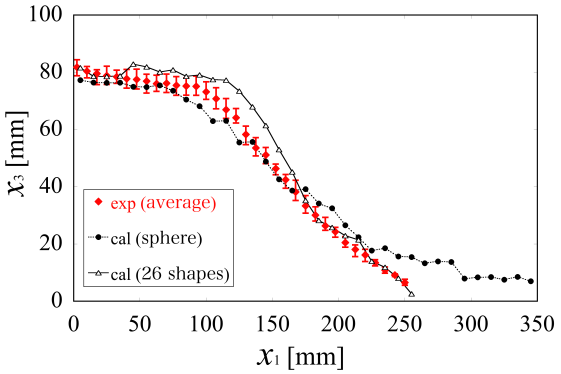

Figure 12. Comparison of particle bed heights

3.3. Particle Transportations due to Falling Water

Hydraulics experiments were conducted to measure the transportation of gravel particles due to falling water from a weir. Figure 13 shows the experimental equipment, in which the supplied water from a pomp overflows a rectangular-notch weir. The falling water impacts on the gravel bed shown as the region-B in Fig. 13, which consists of about 17,000 gravel particles initially placed flat under the still water. The water was supplied during 4 seconds. During and after this period, the dynamic and static behaviors of the gravel particles were observed. The measurements were made with two high-speed digital video cameras and a device similar to point gauges to measure the static gravel bed profiles. Taking account of the variations in experiments, 8 times measurements were conducted in the same hydraulics conditions in order to obtain the averaged shapes of the scoured gravel bed profiles. Since the equivalent diameter of the actual gravel particles is about 4 [mm], the experimental uncertainty is of the same order as this value.

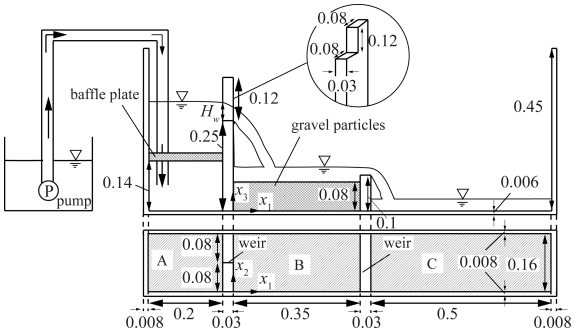

Figure 13. Experimental equipment (unit [m], top: side view, bottom: plan view)

Figure 14 shows the schematic view of the computational conditions. It was confirmed that the calculated time history of the water depth on the top of the weir was in good agreement with the experimental results. The flow rate of the inlet and outlet surfaces in Fig. 14 were given by Dirichlet boundary conditions, while non-slip conditions were employed for the velocity components parallel to the other wall boundaries. The pressure gradients were set $\partial p/\partial n = 0$ on the boundaries except the top and bottom surfaces where the pressure gradients were set equal to the gravitational acceleration.

The numbers of the computational cells were 506×104×258 in $x_1 \times x_2 \times x_3$ directions respectively. Thus, the volumetric grid resolution is about 130, which means the volume ratio of a single particle of the average size to the fluid cell as stated in section 2.5 in this paper. Taking account of the results in section 2.5, since the present volumetric grid resolution of 130 is larger than 78.5 as stated in section 2.5, the grid resolution is sufficient to solve the transportation of the gravel particles. The number of processes in parallel computations was 552 with flat MPI [15] using supercomputer system in Kyoto University.

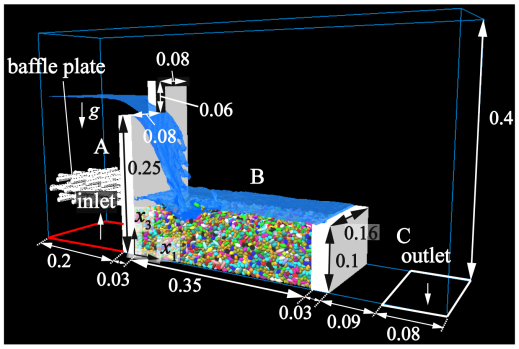

Figure 14. Computational conditions (unit [m])

3.4. Results and Discussion

Figure 15 shows the snapshots of falling water flows and distributions of gravel particles obtained in the experiments and calculations. Three figures on the right hand side in Fig. 15 indicate the computational results obtained only in the range of $0 \leq x_2 \leq 40$ [mm] so as to easily understand the scoured shapes of the gravel bed and particle behaviors. As shown in Fig. 15, the circulating flows are created in the downstream regions of the falling water flows, where the gravel particles are lifted up and the gravel bed is largely scoured both in experiments and calculations. In addition, the transported gravel particles are deposited around the scoured region in the stationary results after the supply of water as shown in Fig. 15 (c).

Figure 16 (a) shows the comparisons of particle bed heights obtained in steady states. In the computations, two different initial distributions of solid models were set up and the final results are indicated as “case1” and “case2” in Fig. 16. It can be seen that the calculated results with different initial conditions on particle configurations are slightly different. In addition, it is shown that the predicted bed profiles, including the lowest and highest levels and gradients of the slopes, reasonably agree with the experimental results in Fig. 16 (a). To compare the profile itself, Fig. 16 (b) shows the distributions, in which experimental results are shifted by 25 [mm] in x_1 direction. As shown in these results, the good agreement of the essential profiles can be found between experiments and numerical predictions.

In addition to the bed profiles in streamwise x_1 direction shown in Fig. 16, their two-dimensional distributions on $x_1 - x_2$ plane are compared in this study. The experimental results in x_2 direction were newly measured in this study, which were not included in our previous paper [1]. The numeric values in Fig. 17 stand for the differences from the initial heights both in experiments and calculations; the negative values mean scoured areas and positive ones are the deposition of gravel particles. In the experiments, five times of measurements were conducted in the same hydraulics conditions, while they might include about 4 [mm] uncertainty taking account that the equivalent diameter of the gravel particles. The calculated results in Fig. 17 are the averaged values of case1 and case2 shown in Fig. 16. While the numerically predicted regions are slightly narrow in x_2 direction and shifted in x_1 direction as indicated in Fig. 16 (a), it is seen that the tendency of the distributions, including the scoured and deposited regions of the gravel particles, is reasonably predicted with the present method.

4. CONCLUSION

In this study, a parallel computation method with a multiphase model was applied to the transportations of about 17,000 gravel particles with a diameter of about 7mm due to the falling water flow through a weir. In the computation method, phase-averaged governing equations for gas and liquid phases were solved with a finite volume method with some advanced numerical techniques : an implicit C-ISMAC method using 5th-order TVD scheme and a pressure calculation method (C-HSMAC method) to preserve incompressible conditions accurately.

The gravel particle was treated as a solid model in computation, which is represented with multiple tetrahedron elements and contact-detection spheres to estimate contact forces between solid models. In order to take account of the shapes and distributions in the actual gravel particles, the representative 26 types of shapes were determined from the measured results to create solid models used in numerical predictions. The fluid forces acting on solid models are estimated from the pressure and viscous terms included in the momentum equations of the gas and liquid phases. Thus, empirical formulations, such as drag and lift coefficients are not necessary in the present method.

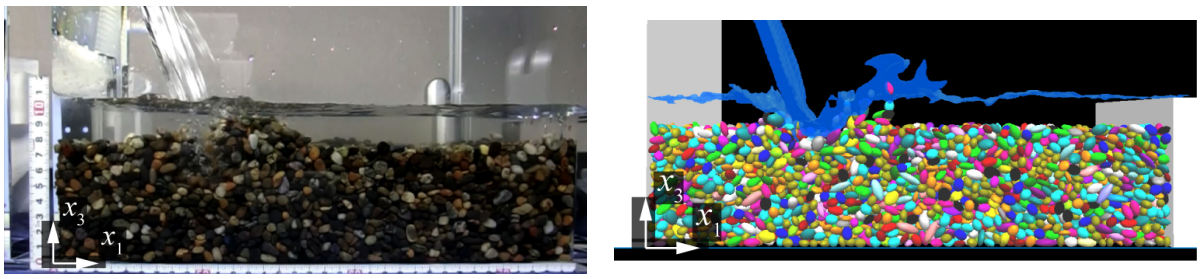

(a) t = 1.07 [s]

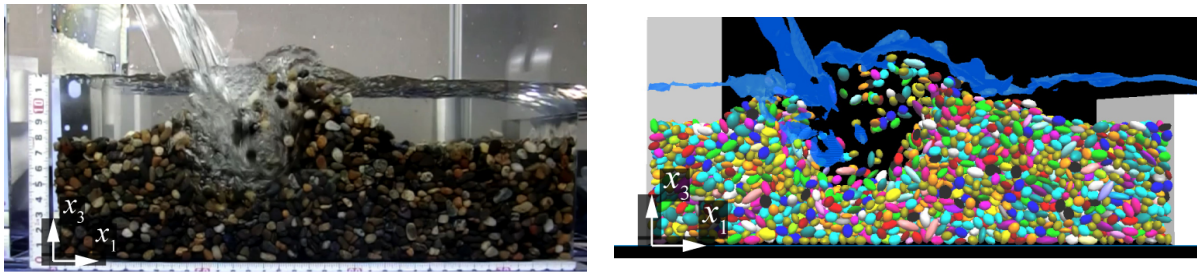

(b) t = 2.65 [s]

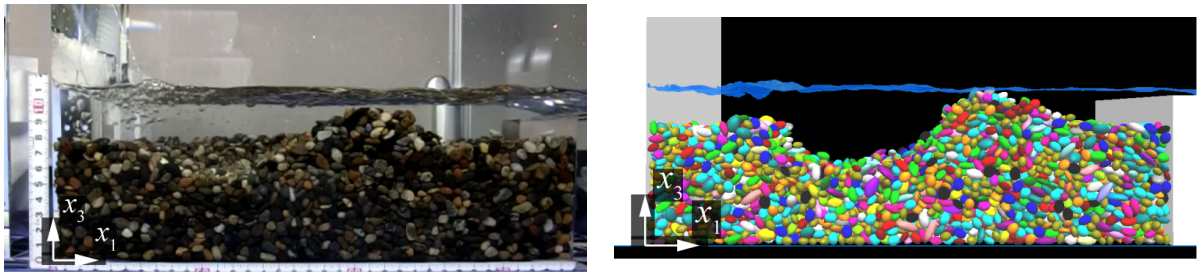

(c) t = 5.27 [s]

Figure 15. Water flows and gravel particles (left: experiments, right: calculations in $0 \leq x_2 \leq 40$ [mm])

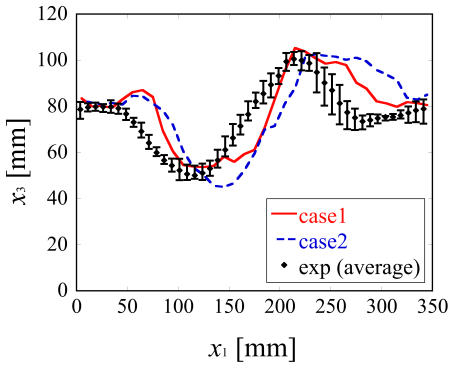

(a) gravel bed heights

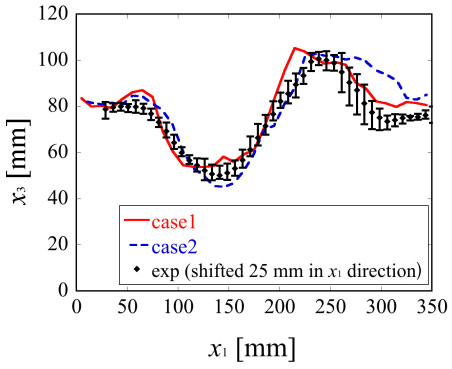

(b) Exp. are shifted by 25 [mm] in x_1 direction

Figure 16. Comparison of gravel bed heights

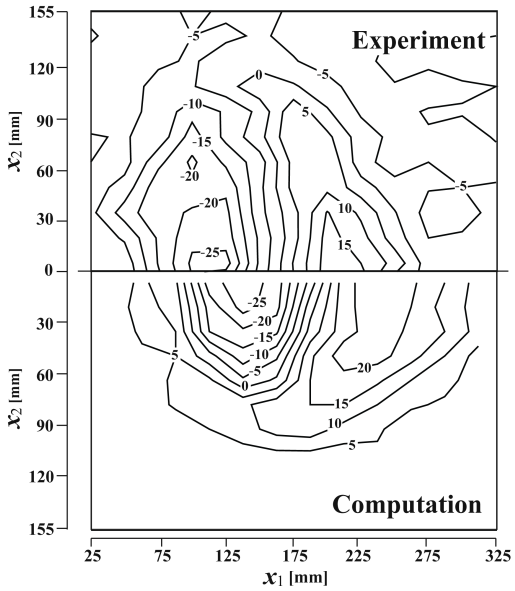

Figure 17. Plan view of gravel bed heights (numerical results are differences from initial values, unit [mm])

In order to confirm the effects of the present 26 types of solid models, angles of repose of gravel particles were calculated with 180 parallel computations and they were compared with the experimental results. As a result, it was shown that the present solid models enable us to obtain the suitable results that agree with experiments, although such results cannot be calculated with the spherical models.

Finally, the present computation method was applied to the deformation of the gravel bed due to overflows from a weir. About 17,000 gravel particles were represented with the present solid model having 26 different shapes and 552 parallel computations were conducted. As a result of computations, it was demonstrated that the dynamic behavior of each gravel particles and the static shapes of the deformed bed heights are reasonably predicted with the present method.

ACKNOWLEDGEMENTS

The authors are grateful to Mr. D. Yagyu, who supported this work when he was a master course student in CERE of the graduate school of engineering in Kyoto University.

REFERENCES

[1] Ushijima, S., Toriu, D., Yanagi, H., and Yagyu, D., 2017, "Computations on transportations of gravel particles due to overflows taking account of particle-particle and particle-fluid mechanical interactions", *Journal of applied mechanics JSCE*, Vol. 73 (2), pp. I_377–I_386.

[2] Ushijima, S., and Kuroda, N., 2009, "3D numerical prediction for interaction between free-surface flows and elastic bodies with MICS and finite element method", *Journal of Hydroscience and Hydraulic Engineering*, Vol. 27 (1), pp. 37–48.

[3] Kidanemariam, A. G., and Uhlmann, M., 2014, "Direct numerical simulation of pattern formation in subaqueous sediment", *Journal of Fluid Mechanics*, Vol. 750, R2.

[4] Fukuoka, S., Fukuda, T., and Uchida, T., 2014, "Effects of sizes and shapes of gravel particles on sediment transports and bed variations in a numerical movable-bed channel", *Advances in Water Resources*, Vol. 72, pp. 84–96.

[5] Ushijima, S., Fukutani, A., and Makino, O., 2008, "Prediction method for movements with collisions of arbitrarily-shaped objects in 3D free-surface flows", *JSCE Journal*, Vol. 64/II-2, pp. 128–138 (in Japanese).

[6] Ushijima, S., and Nezu, I., 2002, "Higher-order implicit (C-ISMAC) method for incompressible flows with collocated grid system", *JSCE Journal*, (719/II-61), pp. 21–30.

[7] Ushijima, S., Okuyama, Y., Takemura, M., and Nezu, I., 2003, "Parallel computational method for pressure field in incompressible flows on 3D curvilinear coordinates", *Annual Journal of Hydraulic Engineering, JSCE*, Vol. 47, pp. 385–390.

[8] Ushijima, S., and Okuyama, Y., 2003, "Comparison of C-HSMAC and SOLA methods for pressure computation of incompressible fluids", *JSCE Journal*, (747/II-65), pp. 197–202.

[9] Ushijima, S., and Kuroda, N., 2009, "Multiphase modeling to predict finite deformations of elastic objects in free surface flows", *Fluid Structure Interaction V, WIT Press*, pp. 34–45.

[10] Yamamoto, S., and Daiguji, H., 1993, "Higher-order-accurate upwind schemes for solving the compressible Euler and Navier-Stokes equations", *Computers & Fluids*, Vol. 22 (2/3), pp. 259–270.

[11] Ushijima, S., 2007, "Multiphase-model approach to predict arbitrarily-shaped objects moving in free surface flows", *Proc of APCOM'07 – EPMESC XI*, pp. MS41–3–1.

[12] Hirt, C. W., and Cook, J. L., 1972, "Calculating three-dimensional flows around structures and over rough terrain", *J Comput Phys*, Vol. 10, pp. 324–340.

[13] Ushijima, S., Yamada, S., Fujioka, S., and Nezu, I., 2006, "Prediction method (3D MICS) for transportation of solid bodies in 3D free-surface flows", *JSCE Journal*, Vol. 810/II-74, pp. 79–89.

[14] Cundall, P. A., and Strack, O. D. L., 1979, "A discrete numerical model for granular assemblies", *Geotechnique*, Vol. 29 (1), pp. 47–65.

[15] Gropp, W., Lusk, E., and Thakur, R., 1999, *Using MPI-2*, The MIT Press.

[16] Chen, S. S., 1988, *Flow-Induced Vibration of Circular Cylindrical Structures*, Hemisphere.

[17] Ushijima, S., Yoshikawa, N., and Yoneyama, N., 2009, "Numerical prediction for fluid forces acting on 3D complicated-shaped objects in free-surface flows", *Journal of Hydroscience and Hydraulic Engineering*, Vol. 27 (1), pp. 23–35.